JOURNAL OF THEORETICAL
AND APPLIED MECHANICS
https://doi.org/10.15632/jtam-pl/224523
ONLINE FIRST

DYNAMIC INSTABILITY ANALYSIS OF POROUS SIGMOID FUNCTIONALLY GRADED TRUNCATED CONICAL SHELLS SUBJECTED TO COMBINED PRESSURES

Xiao-lin HUANG[1], Haoyuan LIU[1], Yuting HAN[1], Yuhua WEI[1], Wei WU[2*]

[1] *School of Architecture and Transportation Engineering, Guilin University of Electronic Technology, Guilin, China*
[2] *School of Physics and Telecommunication, Yulin Normal University, Yulin, China*

*corresponding author, *hxl-68@163.com*

An improved model for assessing the material properties of porous sigmoid functionally graded (S-FGM) conical shells is introduced. Governing equations are derived within thin-shell theory, incorporating static hydraulic pressure, axial periodic loading, and a Winkler–Pasternak foundation. Critical frequencies and unstable regions are obtained via the Galerkin and Bolotin methods. Parametric studies show that the critical frequency decreases with higher porosity, half-vertex angle, or radius-thickness ratio, but increases with ceramic content or foundation stiffness. Porosity fraction and static axial loading notably affect instability regions, while hydraulic pressure has a negligible effect.

Keywords: dynamic stability; buckling; conical shell; sigmoid functionally graded materials; pores.

1. Introduction

Due to their outstanding advantages of light weight, high strength, and high temperature resistance, functionally graded materials (FGMs) have been applied in various engineering structures. Over the past two decades, the stability analysis of FGM shell structures has attracted substantial research attention. Sofiyev (2009; 2016) conducted extensive investigations to analyze the stability of FGM truncated conical shells subjected to various loads and resting on elastic foundations. They found that the material volume fraction, foundation parameters, half-vertex angle, radius-to-thickness ratio, length-to-radius ratio, and environmental temperature exert remarkable effects on buckling pressures. Naj *et al.* (2008) carried out an investigation into the thermal and mechanical instability of FGM conical shells. The results demonstrated that the critical buckling temperature decreases with the increase in the half-vertex angle and ratios of radius to thickness and length to thickness. Also, the discrepancies in the critical temperatures between an FGM and a homogeneous conical shell were discussed in detail. Zhang and Li (2010) explored the dynamic buckling responses of FGM truncated conical shells under normal impact loads. The results illustrated that the material gradient index imposes a significant influence on the critical buckling load. Duc *et al.* (2018) employed the Galerkin integral method combined with the smeared stiffener technique to examine the stability of stiffened FGM conical shells under mechanical loads and surrounded by elastic media. They found that FGM stiffeners improve shell stability far more effectively than homogeneous stiffeners. To address the nonlinear dynamic buckling of FGM toroidal shell segments, Ali and Hasan (2019) utilized Galerkin's integral technique, the Budiansky–Roth criterion, and the Runge–Kutta iterative approach to determine the nonlinear static and dynamic buckling loads. It was revealed that a higher loading velocity leads to a larger critical buckling load. Fan *et al.* (2021) studied the dynamic stability of magnetostrictive-face-bonded FGM conical microshells while accounting for

nonlinear cubic stiffness and viscoelastic foundation effects. The results showed that the natural frequency rises within the prebuckling region under a fixed axial load. In contrast, it was reduced in the postbuckling domain. Yuan *et al.* (2021) investigated the dynamic stability of FGM conical microshells combined with magnetostrictive facesheets. They found that a larger material gradient index reduces the natural frequency in the prebuckling stage. Moreover, Nemati and Mahmoodabadi (2020) analyzed how different micromechanical models affect the stability of FGM conical panels exposed to various thermal fields. Despite abundant existing research focusing on the buckling analysis of FGM conical shells, studies concerning their dynamic stability are relatively scarce.

All the above-cited literature assumes that shell structures are perfect and free of internal pores. In reality, internal pores are inevitably generated inside material substrates (Mallek *et al.*, 2025; Wu *et al.*, 2020; Zhu *et al.*, 2001). Consequently, some studies have been conducted to examine how these internal pores affect the stability of FGM conical shells. Allahkarami *et al.* (2020) integrated the generalized differential quadrature method with Bolotin's approach to determine the dynamic instability region of a bi-directional FGM truncated conical shell, in which multiple boundary conditions and elastic foundations were taken into consideration. Fu *et al.* (2021) quantified the pore effect on the upper and lower bounds of the dynamic instability regions. Hoa *et al.* (2022) discussed the impact of internal pores on the critical buckling load of FGM conical shells. All these investigations revealed that the presence of internal pores significantly influences both the critical buckling load and the dynamic instability region of porous shell structures. Another notable limitation of the material property models adopted in these papers lies in their questionable basic assumption: they presume the pore volume fraction is sufficiently small and can be neglected when calculating the total volume of shell components.

Sigmoid functionally graded materials (S-FGMs) are advanced subclasses of FGMs, distinguished by their distinctive three-layer ceramic–metal–ceramic gradient configuration, in which the material fractions vary smoothly along the thickness direction following a sigmoid function (Chi & Chung, 2006). Unlike conventional FGM, S-FGM proves to be particularly effective in alleviating stress concentrations at interfaces where material properties would otherwise change abruptly, thereby remarkably enhancing structural integrity under various loading conditions. Due to these superior advantages, S-FGM truncated conical shells are increasingly considered for critical applications in aerospace, marine, and mechanical engineering such as rocket adapters, submarine pressure hulls, and aircraft fuselage components where lightweight design and high load-bearing capacity are paramount. In these demanding applications, the structures are frequently subjected to complex combined loads such as axial compression, external pressure, and thermal loads. Therefore, a thorough understanding of the buckling and dynamic characteristics of porous S-FGM conical shells under such conditions is essential for reliable and damage-tolerant engineering design. However, despite their evident practical significance, only a handful of publications have reported the static and dynamic mechanical behaviors of S-FGM truncated conical shells, particularly regarding dynamic stability analysis under combined loads (Bich & Ninh, 2016; Duc & Cong, 2015; Foroutan & Torabi, 2026; Pal *et al.*, 2025).

The foregoing literature review reveals that research regarding the dynamic stability of S-FGM conical shells is still limited. To the best knowledge of the authors, no previous study has explored the dynamic stability of porous S-FGM truncated shells, especially those with specific pore distribution patterns and under combined multi-type loads. Additionally, the literature review demonstrates that the previous model for assessing the properties of porous S-FGM materials overlooked the influence of the porosity volume on the total volume of S-FGM shells. To fill these research gaps, the present study proposes an improved model for S-FGM material properties and conducts a systematic analysis of the dynamic stability characteristics of porous S-FGM truncated conical shells under simply supported boundary conditions, subjected to combined static hydraulic pressure, axial periodic loading, and a Winkler–Pasternak elastic foundation.

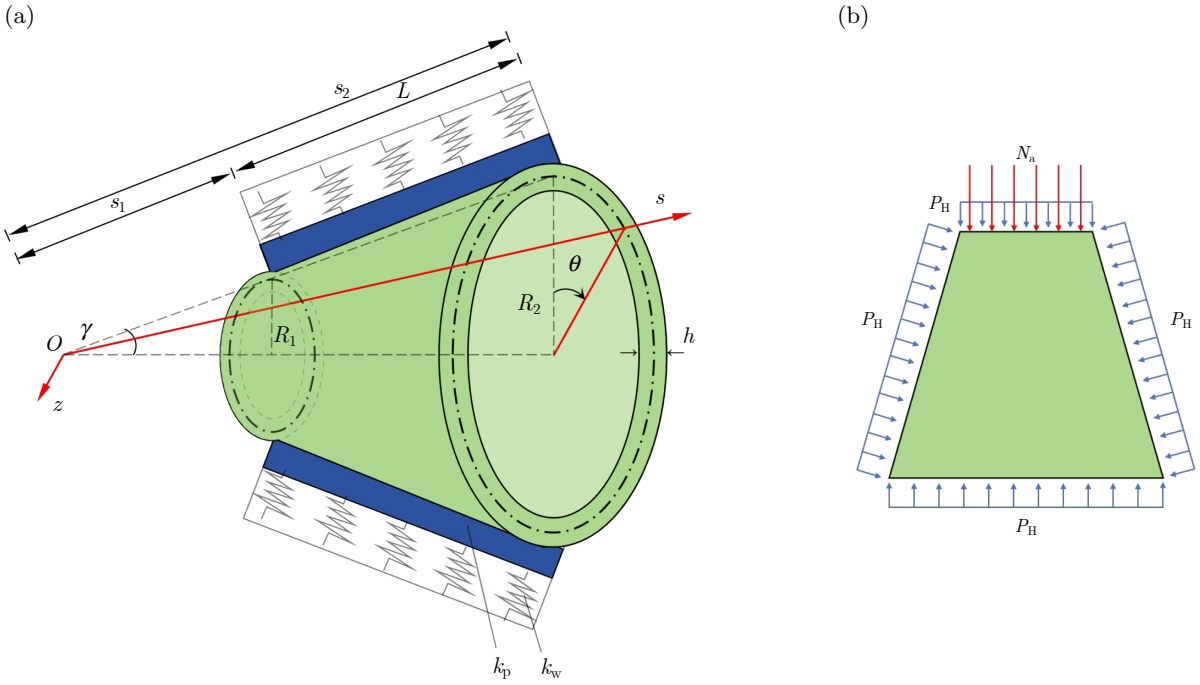

Fig. 1. S-FGM truncated conical shell surrounded by (a) an elastic medium and subjected to (b) hydraulic and axial pressures.

2. Theory analysis

Consider an S-FGM truncated conical thin shell composed of ceramic and metal, as depicted in Fig. 1. The shell is subjected to a static hydraulic pressure P_{H} along with a periodic axial pressure N_{a}. A curvilinear coordinate system (s, Θ, z) is introduced on the middle surface, where s denotes the meridional distance from the virtual apex, θ is the circumferential coordinate (positive clockwise viewed from the apex), and z is the inward normal coordinate. Let s_1 and s_2 be the distances from the virtual apex to the mid-surface of the smaller and larger bases, with corresponding radii R_1 and R_2, respectively. The geometric parameters L, h, and γ represent the length, thickness, and half-cone angle of the shell.

It is assumed the shell is supported by a Winkler–Pasternak foundation. By introducing the variable $\psi = \theta sin\gamma$, the reaction of the foundation to the shell is calculated as

$$p_{\mathrm{f}} = k_{\mathrm{w}} W - k_{\mathrm{p}} \left(\frac{\partial^2 W}{\partial s^2} + \frac{1}{s} \frac{\partial^2 W}{\partial s \partial \psi} + \frac{1}{s^2} \frac{\partial^2 W}{\partial \psi^2} \right), \tag{2.1}$$

in which p_{f} is the force per unit area, k_{w} and k_{p} are the parameters of the Winkler foundation normal stiffness and the Pasternak foundation shear stiffness, respectively. Additionally, W is the displacement along the thickness direction.

According to Hooke's law and the linear strain-displacement relationship of the shell, the normal stresses σ_s, σ_θ, and shear stress $\sigma_{z\theta}$ of the shell are given by Eq. (2.2):

$$\begin{pmatrix} \sigma_s \\ \sigma_\theta \\ \sigma_{s\theta} \end{pmatrix} = \frac{\widehat{E}(z)}{1-\widehat{\nu}^2(z)} \begin{bmatrix} 1 & \widehat{\nu}(z) & 0 \\ \widehat{\nu}(z) & 1 & 0 \\ 0 & 0 & \dfrac{1-\widehat{\nu}(z)}{2} \end{bmatrix} \times \begin{bmatrix} \varepsilon_s - z \dfrac{\partial^2 W}{\partial s^2} \\ \varepsilon_\theta - z \left(\dfrac{1}{s^2} \dfrac{\partial^2 W}{\partial \psi^2} + \dfrac{1}{s} \dfrac{\partial W}{\partial s} \right) \\ \varepsilon_{s\theta} - z \left(\dfrac{1}{s} \dfrac{\partial^2 W}{\partial s \partial \psi} - \dfrac{1}{s^2} \dfrac{\partial W}{\partial \psi} \right) \end{bmatrix}, \tag{2.2}$$

where ε_s, ε_θ, and $\varepsilon_{s\theta}$ imply the strains in the middle curved surface, W is the normal displacement, $\widehat{E}(z)$ and $\widehat{\nu}(z)$ represent the effective elastic modulus and Poisson's ratio.

The moments M_s, M_θ, and $M_{s\theta}$ are computed as follows:

$$(M_s, M_\theta, M_{s\theta}) = \int_{-h/2}^{h/2} (\sigma_s, \sigma_\theta, \sigma_{s\theta}) z dz. \tag{2.3}$$

The membrane forces N_s, N_θ, and $N_{s\theta}$ can be computed using the Airy function F as

$$(N_s, N_\theta, N_{s\theta}) = \left(\frac{1}{s^2}\frac{\partial^2 F}{\partial \psi^2} + \frac{1}{s}\frac{\partial F}{\partial s}, \quad \frac{\partial^2 F}{\partial s^2}, \quad -\frac{1}{s}\frac{\partial^2 F}{\partial s \partial \psi} + \frac{1}{s^2}\frac{\partial F}{\partial \psi} \right). \tag{2.4}$$

In this research, some internal pores are assumed to exist in the shell. As depicted in Fig. 2, the even and uneven distributions are taken into account.

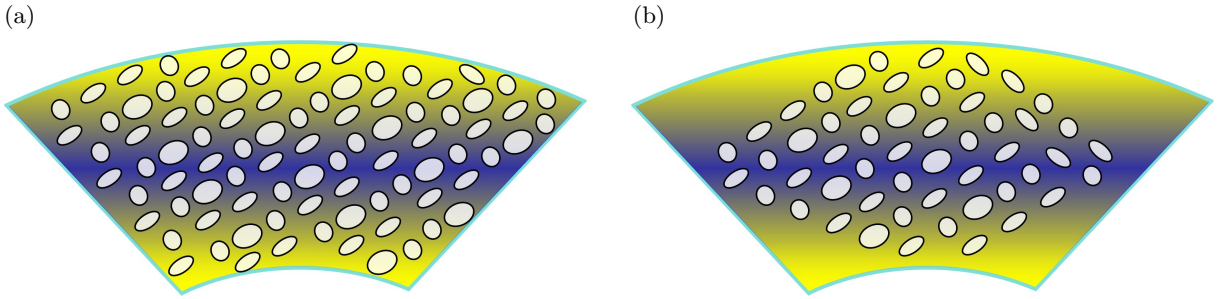

Fig. 2. Porosity distribution: (a) even distribution; (b) uneven distribution.

In the previous research on porous FGM structures, the porosity volume fraction $\overline{\alpha}$ is usually regarded as a tiny variable ($\overline{\alpha} \ll 1$). Hence, $\overline{\alpha}$ can be neglected, and the total volume of porous structures is computed as $\overline{V}_\mathrm{c} + \overline{V}_\mathrm{m} = 1$, where $\overline{V}_\mathrm{c}$ and $\overline{V}_\mathrm{m}$ are the total volume fractions of ceramic and metal, respectively. However, the assumption is inaccurate. To remove the assumption, the equations of computing the total volume and mass fractions of the shell are introduced as $\overline{V}_\mathrm{c} + \overline{V}_\mathrm{m} + \overline{\alpha} = 1$ and $W_\mathrm{c} + W_\mathrm{m} = 1$, where W_c and W_m imply the mass fractions of ceramic and metal. Thus, $\overline{V}_\mathrm{c}$ can be calculated by

$$\overline{V_\mathrm{c}} = (1 - \overline{\alpha}) \frac{W_\mathrm{c}/\rho_\mathrm{c}}{W_\mathrm{c}/\rho_\mathrm{c} + W_\mathrm{m}/\rho_\mathrm{m}}, \tag{2.5}$$

where ρ_c and ρ_m imply the mass densities of ceramic and metal, respectively.

The ceramic volume fraction $V_\mathrm{c}(z)$ for S-FGM is supposed to be (Duc & Cong, 2015; Naj *et al.*, 2008):

$$V_\mathrm{c}(z) = \begin{cases} V_{\mathrm{c}1}^* \left(1 - \frac{1}{2}\left(1 - \frac{2z}{h} \right)^N \right), & (0 \le z \le h/2), \\ \frac{1}{2} V_{\mathrm{c}1}^* \left(1 + \frac{2z}{h} \right)^N, & (-h/2 \le z \le 0), \end{cases} \tag{2.6}$$

and that for typical FGMs is given by

$$V_\mathrm{c}(z) = V_{\mathrm{c}2}^* \left(1 + \frac{2z}{h} \right)^N, \tag{2.7}$$

where N is the volume fraction index.

Assuming that the total ceramic volume is equivalent for the two porosity distributions, the coefficients V_{c1}^* and V_{c2}^* can be determined by

$$\int_{-h/2}^{0} \frac{1}{2} V_{c_1}^* \left(1 + \frac{2z}{h}\right)^N dz + \int_{0}^{h/2} V_{c_1}^* \left[1 - \frac{1}{2}\left(1 - \frac{2z}{h}\right)^N\right] dz = \overline{V}_c h, \tag{2.8}$$

$$\int_{-h/2}^{h/2} V_{c_2}^* \left(1 + \frac{2z}{h}\right)^N dz = \overline{V}_c h. \tag{2.9}$$

Following the rule of mixtures, the effective values of the elastic modulus $\widehat{E}(z)$, mass density $\widehat{\rho}(z)$, and Poisson's ratio $\widehat{\nu}(z)$ are given by

$$\widehat{E}(z) = E_c V_c(z) + E_m\big(1 - V_c(z) - \alpha(z)\big), \tag{2.10}$$

$$\widehat{\rho}(z) = \rho_c V_c(z) + \rho_m\big(1 - V_c(z) - \alpha(z)\big), \tag{2.11}$$

$$\widehat{\nu}(z) = \nu_c V_c(z) + \nu_m\big(1 - V_c(z) - \alpha(z)\big), \tag{2.12}$$

where E_c and ν_c represent the elastic modulus and Poisson's ratio of the ceramic, respectively, while E_m and ν_m denote those of the metal. In the case of both even (ED) and uneven (UD) porosity distributions, the volume distribution $\alpha(z)$ is assumed to be

$$\alpha(z) = \overline{\alpha}, \qquad \text{(ED)}, \tag{2.13}$$

$$\alpha(z) = \alpha^* \left(1 - \frac{2|Z|}{h}\right), \qquad \text{(UD)}. \tag{2.14}$$

It is supposed that the total porosity volumes for the two distributions are equivalent. The coefficient α^* is calculated by

$$\int_{-h/2}^{h/2} \alpha^* \left(1 - \frac{2|z|}{h}\right) dz = \overline{\alpha}\, h. \tag{2.15}$$

Subjected to hydraulic pressure P_H and periodical axial pressure N_a at the smaller end of the shell, the initial membrane forces of the shell can be obtained as follows (Sofiyev, 2010):

$$\begin{aligned} N_s^0 &= -0.5 P_H s \tan\gamma - 0.5 N_a s_2^2 \tan\gamma / s, \\ N_\theta^0 &= -P_H s \tan\gamma, \qquad N_{s\theta}^0 = 0. \end{aligned} \tag{2.16}$$

Employing Hamilton's principle, after a long computation, the equations of dynamic equilibrium and the deformation compatibility of the shell can be deduced as follows (Ng *et al.*, 2001; Sofiyev & Schnack, 2012):

$$\begin{aligned} &\frac{\partial^2 M_s}{\partial s^2} + \frac{2}{s}\frac{\partial M_s}{\partial s} + \frac{2}{s}\frac{\partial^2 M_{s\theta}}{\partial s \partial \psi} - \frac{1}{s}\frac{\partial M_\theta}{\partial s} + \frac{2}{s^2}\frac{\partial M_{s\theta}}{\partial \psi} + \frac{1}{s^2}\frac{\partial^2 M_\theta}{\partial \psi^2} + \frac{N_\theta}{s}\cot\gamma \\ &\quad + \frac{N_\theta^0}{s}\left(\frac{1}{s}\frac{\partial^2 W}{\partial \psi^2} + \frac{\partial W}{\partial s}\right) + N_s^0 \frac{\partial^2 W}{\partial s^2} + 2N_{s\theta}^0 \frac{\partial}{\partial s}\left(\frac{1}{s}\frac{\partial W}{\partial \psi}\right) - \rho_f h \frac{\partial^2 W}{\partial t^2} \\ &\quad - k_w W + k_p\left(\frac{\partial^2 W}{\partial s^2} + \frac{2}{s}\frac{\partial^2 W}{\partial s \partial \psi} + \frac{1}{s^2}\frac{\partial^2 W}{\partial \psi^2}\right) = 0, \end{aligned} \tag{2.17}$$

$$\frac{\cot\gamma}{s}\frac{\partial^2 W}{\partial s^2}-\frac{2}{s}\frac{\partial^2\varepsilon_{s\theta}}{\partial s\partial\psi}-\frac{2}{s^2}\frac{\partial\varepsilon_{s\theta}}{\partial\psi}+\frac{\partial^2\varepsilon_{\theta}}{\partial s^2}+\frac{1}{s^2}\frac{\partial^2\varepsilon_{s}}{\partial\psi^2}+\frac{2}{s}\frac{\partial\varepsilon_{\theta}}{\partial s}-\frac{1}{s}\frac{\partial\varepsilon_{s}}{\partial s}=0, \quad (2.18)$$

where $\rho_{\mathrm{f}}=\int_{-0.5h}^{0.5h}\widehat{\rho}(z)dz$ is the mass inertia.

Introducing two variables $x=\ln(s/s_1)$ and $F_1=Fe^{-2x}$, then substituting Eqs. (2.2), (2.3), (2.4), and (2.16) into Eqs. (2.17) and (2.18), the governing equations of the dynamic stability for the shell can be rewritten as follows:

$$T_{11}(F_1)+T_{12}(W)+P_{\mathrm{H}}T_{13}(W)+N_{\mathrm{a}}T_{14}(W)-\rho_{\mathrm{f}}hs_1^4e^{4x}\frac{\partial^2 W}{\partial t^2}=0, \quad (2.19)$$

$$T_{21}(F_1)+T_{22}(W)=0, \quad (2.20)$$

in which the differential operators $T_{ij}(\ )$ are given in Appendix (A.1).

The two bases of the shell are supposed to be simply supported. The boundary conditions can be written as

$$s=s_1,\ s_2: \quad W=M_s=0. \quad (2.21)$$

The satisfaction of boundary conditions requires that the displacements W take the form:

$$W=\sum_m\sum_n w_{mn}(t)e^x\sin(\beta_1 x)\sin(\beta_2\psi), \quad (2.22)$$

where the coefficients β_1 and β_2 are defined by

$$\beta_1=\frac{m\pi}{x_0},\qquad \beta_2=\frac{n}{\sin\gamma},\qquad x_0=\ln(s_2/s_1), \quad (2.23)$$

in which m and n represent the meridional half and circumferential wave numbers, respectively.

Substituting Eq. (2.22) into Eq. (2.20), then employing the superposition principle, the Airy function F_1 can be obtained as

$$F_1=\sum_m\sum_n f_{mn}(t)(\mu_1\sin\beta_1 x+\mu_2\cos\beta_1 x+\mu_3e^{-x}\sin\beta_1 x+\mu_4e^{-x}\cos\beta_1 x)\sin\beta_2\psi, \quad (2.24)$$

in which $\mu_i(i=1-4)$ are the constant coefficients.

The axial periodic pressure N_{a} is assumed to be

$$N_{\mathrm{a}}(t)=N_0(\mu_{\mathrm{s}}+\mu_{\mathrm{d}}\cos\varphi t), \quad (2.25)$$

where μ_{s} and μ_{d} represent the static and dynamic coefficients of the periodical pressure, φ is the excitation frequency.

Substituting Eqs. (2.22), (2.24), and (2.25) into Eq. (2.19), then multiplying Eq. (2.19) by $\sin\beta_1 x\sin\beta_2\psi$ and using Galerkin's integral technique in the ranges $0\le\psi\le 2\pi\sin\gamma$ and $0\le x\le x_0$, the differential equations can be deduced as follows:

$$\mathbf{M}\ddot{\chi}+(\mathbf{K}_0+P_{\mathrm{H}}\mathbf{K}_{\mathrm{P}}+\mu_{\mathrm{s}}N_0\mathbf{K}_{\mathrm{G}})\chi+(\mu_{\mathrm{d}}N_0\mathbf{K}_{\mathrm{G}}\cos\varphi\mathrm{t})\chi=0, \quad (2.26)$$

in which $\mathbf{M}$, $\mathbf{K}_0$, $\mathbf{K}_{\mathrm{P}}$, and $\mathbf{K}_{\mathrm{G}}$ are the matrices of mass, stiffness, hydraulic pressure, and geometric stiffness. $\chi=\{w_{mn}(t)\}$ represents the displacement vector.

Let $\chi=\{A\}e^{iwt}$ and $N_0=0$. Equation (2.26) is reformed as

$$\left((\mathbf{K}_0+P_{\mathrm{H}}\mathbf{K}_{\mathrm{P}})-\omega^2\mathbf{M}\right)\chi=0. \quad (2.27)$$

Based on Eq. (2.27), the natural frequencies ω can be solved. It is noted that the frequency ω varies with hydraulic pressure P_{H}. When $\omega = 0$, the critical hydraulic pressure P_{Hcr} can be attained.

The dynamic stability of the shell can be described by the Mathieu-Hill type differential Eq.(2.26). To identify the points on the edges of unstable regions, the Bolotin method is adopted. The assumed solution of Eq. (2.26) can be expanded by using a series of trigonometric functions containing the excitation frequency φ as follows (Ng *et al.*, 2001):

$$\chi = \sum_{k=1.3\ldots} \left(f_k \sin \frac{k\varphi t}{2} + g_k \cos \frac{k\varphi t}{2} \right), \tag{2.28}$$

with period $2T$, where $T = 2\pi/\varphi$, or

$$\chi = \frac{g_0}{2} + \sum_{k=2.4\ldots} \left(f_k \sin \frac{k\varphi t}{2} + g_k \cos \frac{k\varphi t}{2} \right), \tag{2.29}$$

with period T, where $T = 2\pi/\varphi$, f_k and g_k are the constant coefficients. The principal unstable regions with $2T$ are usually wider than those with T and are of greater practical importance (Bich & Ninh, 2016). Therefore, the solutions with $2T$ are considered in this research. Substituting Eq. (2.28) into Eq. (2.26) and assembling the $\sin(k\varphi t/2)$ and $\cos(k\varphi t/2)$ terms, a group of linear homogeneous algebraic equations in terms of f_k and g_k can be deduced. In general, a solution sufficiently accurate may be found using the first-order approximation with $k = 1$. To obtain a non-trivial solution, the following conditions need to be satisfied:

$$\det \left| \left(\mathbf{K}_0 + P_{\mathrm{H}}\mathbf{K}_{\mathrm{P}} + \mu_{\mathrm{s}} N_0 \mathbf{K}_{\mathrm{G}} - \frac{1}{2}\mu_{\mathrm{d}} N_0 \mathbf{K}_{\mathrm{G}} - \frac{\varphi^2}{4}\mathbf{M} \right) \right| = 0, \tag{2.30}$$

$$\det \left| \left(\mathbf{K}_0 + P_{\mathrm{H}}\mathbf{K}_{\mathrm{P}} + \mu_{\mathrm{s}} N_0 \mathbf{K}_{\mathrm{G}} + \frac{1}{2}\mu_{\mathrm{d}} N_0 \mathbf{K}_{\mathrm{G}} - \frac{\varphi^2}{4}\mathbf{M} \right) \right| = 0. \tag{2.31}$$

If the values of the static hydraulic pressure P_{H} and axial loading $\mu_{\mathrm{s}} N_0$ are given, the two critical excitation frequencies at every dynamic pressure level $\beta = \mu_{\mathrm{d}}/\mu_{\mathrm{s}}$ can be found by solving Eqs. (2.30) and (2.31). By introducing the dimensionless external frequency $\phi = 2\pi\varphi(\rho_{\mathrm{m}}/E_{\mathrm{m}})^{0.5}$, the two curved lines in the $\phi - \beta$ plane with a common point at $\beta = 0$ form the boundary lines between the stable and unstable regions.

If $\gamma \to 0$, $s_1 \to \infty$, $s_1 \sin\gamma = R$, $\ln(s_1/s_2)\sin\gamma = R/L$, the results for a conical shell are converted into those for the corresponding cylindrical shell (Sofiyev & Schnack, 2012).

3. Results and discussion

3.1. Verification

To validate the effectiveness and accuracy of the present approach, the following three numerical examples of investigating the buckling and dynamic instability for typical FGM conical shells are presented:

Example 1. Table 1 compares the results of critical hydraulic pressure P_{Hcr} for a typical Si_3N_4/SUS304 FGM conical shell with those given by Sofiyev (2009). The elastic modulus, mass density, and Poisson's ratio for Si_3N_4 are $E_{\mathrm{c}} = 322.27\,\mathrm{GPa}$, $\rho_{\mathrm{c}} = 2370\,\mathrm{kg/m^3}$, and $\nu_{\mathrm{c}} = 0.24$, and those for SUS304 are $E_{\mathrm{m}} = 207.7877\,\mathrm{GPa}$, $\rho_{\mathrm{m}} = 8166\,\mathrm{kg/m^3}$, and $\nu_{\mathrm{m}} = 0.317756$. The adopted geometric parameters are $R_1 = 1.0\,\mathrm{m}$, $R_2 = 3.0\,\mathrm{m}$, $R_2/h = 300$, and $\gamma = 30^\circ$. The meridional half-wave number is $m = 1$, while the circumferential wave numbers n are presented in Table 1. It is clear that the present results are almost the same as those presented by Sofiyev (2009).

Table 1. Comparison of critical hydraulic pressures $P_{\mathrm{Hcr}}(n)$ [MPa].

Method	Si_3N_4	$N = 1.0$	$N = 2.0$	SUS304
Sofiyev (2009)	0.257(8)	0.200(8)	0.191(8)	0.155(7)
Present	0.253(8)	0.197(8)	0.187(8)	0.153(7)

Example 2. The dimensionless fundamental frequency Ω for a typical Si_3N_4/Ni FGM conical shell encircled by Winkler–Pasternak elastic medium is shown in Table 2. The material properties for Si_3N_4 are $E_{\mathrm{c}} = 322.27\,\mathrm{GPa}$, $\rho_{\mathrm{c}} = 2370\,\mathrm{kg/m^3}$, and $\nu_{\mathrm{c}} = 0.24$, and those for Ni are $E_{\mathrm{m}} = 205.098\,\mathrm{GPa}$, $\rho_{\mathrm{m}} = 8900\,\mathrm{kg/m^3}$, and $\nu_{\mathrm{m}} = 0.31$. The geometric dimensions are $R_2/h = 100$, $L = 2R_1$, and $\gamma = 30°$. The dimensionless fundamental frequency is defined as $\Omega = \omega R_2 \left((1-\nu_{\mathrm{c}}^2)\rho_{\mathrm{c}}/E_{\mathrm{c}}\right)^{0.5}$. The table illustrates that the present results are very similar to those of Sofiyev *et al.* (2012).

Table 2. Comparison of natural frequency parameter $\Omega(n)$.

k_{w} [N/m^3]	k_{p} [N/m]	Method	Ni	$N = 1.0$	$N = 2.0$	Si_3N_4
0	0	Sofiyev *et al.* (2012)	0.0723(7)	0.0997(7)	0.0887(7)	0.1763(7)
		Present	0.0725(7)	0.1001(7)	0.0891(7)	0.1771(7)
5×10^6	0	Sofiyev *et al.* (2012)	0.0813(7)	0.1103(7)	0.0988(7)	0.1910(7)
		Present	0.0816(7)	0.1112(7)	0.1003(7)	0.1918(7)
5×10^6	2.5×10^5	Sofiyev *et al.* (2012)	0.0888(7)	0.1198(6)	0.1072(6)	0.2046(6)
		Present	0.0892(7)	0.1210(6)	0.1083(6)	0.2061(6)

Example 3. The dimensionless critical excitation frequency $\overline{\phi^*}$ at $\beta = 0$ and for a typical Si_3N_4/Ni FGM cylindrical shell under axial dynamic pressure $N_0 = 0.5N_{\mathrm{cr}}$ are listed in Table 3. The material properties are $E_{\mathrm{c}} = 322.27\,\mathrm{GPa}$, $\rho_{\mathrm{c}} = 2370\,\mathrm{kg/m^3}$, and $\nu_{\mathrm{c}} = 0.24$ for Si_3N_4, and those for Ni are $E_{\mathrm{m}} = 205.098\,\mathrm{GPa}$, $\rho_{\mathrm{m}} = 8900\,\mathrm{kg/m^3}$, and $\nu_{\mathrm{m}} = 0.31$. The critical axial pressure is $N_{\mathrm{cr}} = \frac{E_{\mathrm{m}}h^2}{R\left(3(1-\nu_{\mathrm{m}}^2)\right)^{0.5}}$, and the dimensionless critical excitation frequency is defined by $\overline{\phi^*} = 2\pi R\varphi(\rho_{\mathrm{c}}/A_{11})^{0.5}$. The transverse mode (m, n) is $(1, 1)$, and the material parameters for Si_3N_4 and Ni are the same as those in Example 2. The geometric parameters are $R/h = 100$ and $L/R = 1.0$. It is revealed that the present results are very close to those in (Ng *et al.*, 2001).

Table 3. Comparison of dimensionless critical excitation frequency $\overline{\phi^*}$.

Method	$N = 0$	$N = 0.5$	$N = 1$	$N = 5$	$N = 10$
Ng *et al.* (2001)	10.3932	10.5262	10.5831	10.6736	10.6899
Present	10.4133	10.5507	10.6126	10.7031	10.7052

3.2. Parametric studies

This subsection investigates the influences of internal pores, material constitution, elastic medium, hydraulic pressure, and geometric parameters on the dynamic stability of a porous Si_3N_4/SUS304 S-FGM conical shell. The material parameters are the same as in Example 1. The hydraulic pressure and the amplitude of dynamic loading are, respectively:

$$P_{\mathrm{H}} = 2.96\mu_{\mathrm{H}}\frac{E_{\mathrm{m}}h}{s_2(1-\nu_{\mathrm{m}}^2)^{0.75}}\left(\frac{h}{s_2\tan\gamma}\right)^{1.3}\left(1-0.78(\frac{h}{s_2\tan\gamma})^{0.5}+0.38\frac{h}{s_2\tan\gamma}\right)$$

and

$$N_0 = \frac{E_m h^2}{R\left[3\left(1-\nu_m^2\right)\right]^{0.5}}.$$

The dimensionless excitation frequency is defined as $\phi = 2\pi\varphi(\rho_m/E_m)^{0.5}$. Unless otherwise stated, the following parameters are adopted: $W_c = 0.2$, $\overline{\alpha} = 0.1$, $N = 1.0$, $\gamma = 30°$, $h = 0.01\,\mathrm{m}$, $R_1/h = 100$, $L/R_1 = 1.0$, $k_w = 1.0 \times 10^7\,\mathrm{N/m^3}$, $k_p = 2.5 \times 10^5\,\mathrm{N/m}$, $\mu_H = 0.5$, $\mu_s = 0.5$.

In each unstable region, the boundaries are defined by two lines that originate from a common point on the ϕ-axis. Although these lines appear straight, they are actually very slightly curved. To quantify the size of the unstable region, Ng *et al.* (2001) proposed the subtended angle Θ, as illustrated in Fig. 3. The angle Θ is calculated using the arctangent of the right-angled triangle $\angle AOB$. It provides an accurate measure of the slope of the boundaries of the unstable region, based on calculations involving a similar triangle $\angle A^*OB^*$. Evidently, a larger Θ indicates a wider unsafe frequency band, and ϕ^* denotes the critical excitation frequency at $\beta = 0$. Physically, stable regions correspond to decaying vibrations, while unstable regions imply parametric resonance with exponentially growing amplitudes that risk fatigue or failure.

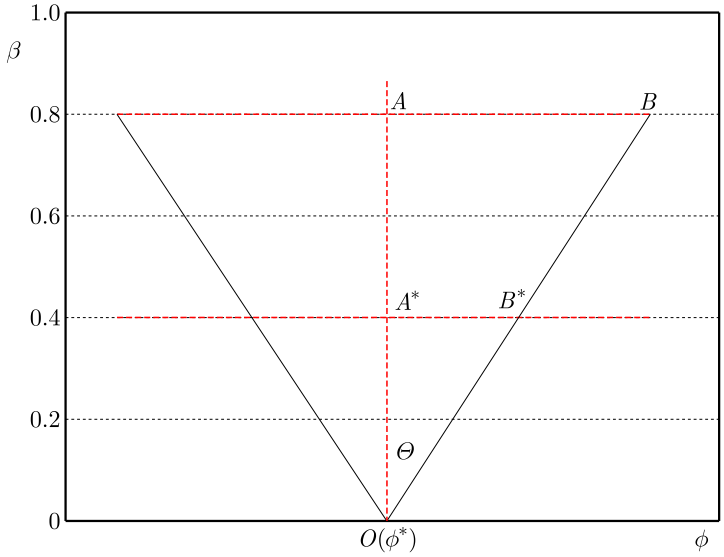

Fig. 3. Unstable region in the $\phi - \beta$ plane.

Figure 4 shows that increasing the wave number n can reduce the value of the critical excitation frequency ϕ^*. As the wave number n changes from 1 to 5, the critical frequency ϕ^* declines from 5.850 to 1.304, and the subtended angle Θ also declines from 31.38° to 8.32°. The change demonstrates that the stability for a lower mode (m, n) is higher than that for a higher mode (m, n).

Figure 5 reveals the influence of porosity distributions. It is found that the critical excitation frequency ϕ^* for UD is higher than that for ED. However, the subtended angle Θ is almost unchanged. This is because the pores for UD are more distributed in the middle area of the conical shell. The stiffness for UD is higher than that for ED.

The influence of the porosity volume fraction $\overline{\alpha}$ is revealed in Fig. 6. Since increasing $\overline{\alpha}$ leads to the lower effective stiffness, the critical excitation frequency ϕ decreases, and the unstable region is expanded. When $\overline{\alpha}$ increases from 0.0 to 0.3, the excitation frequency ϕ^* declines from 5.876 to 5.787. In contrast, the subtended angle Θ rises from 7.56° to 10.86°. Hence, internal pores should be diminished to improve the dynamic stability of the shell in making S-FGMs.

Figure 7 illustrates the influence of the ceramic mass fraction W_c on the dynamic stability. If the mass fraction W_c changes in the range of 0.1 to 0.3, the critical excitation frequency ϕ^* increases from 5.319 to 6.212. Since the elastic modulus of Si_3N_4 is larger than that

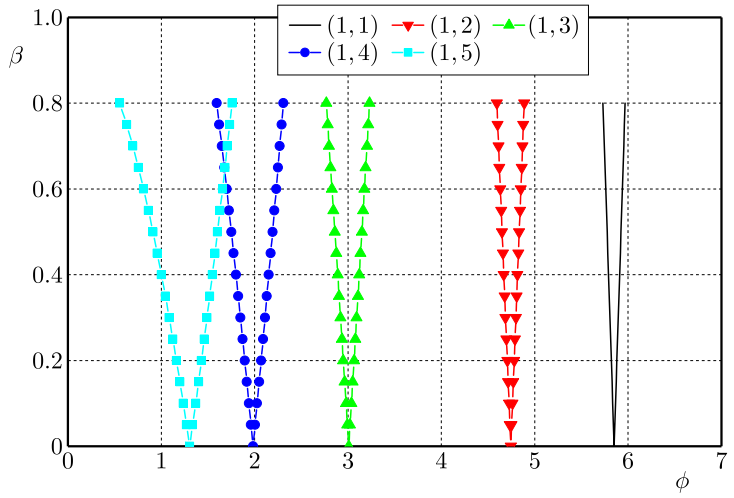

Fig. 4. Influence of transverse modes (m, n) on the dynamic stability of a porous S-FGM conical shell.

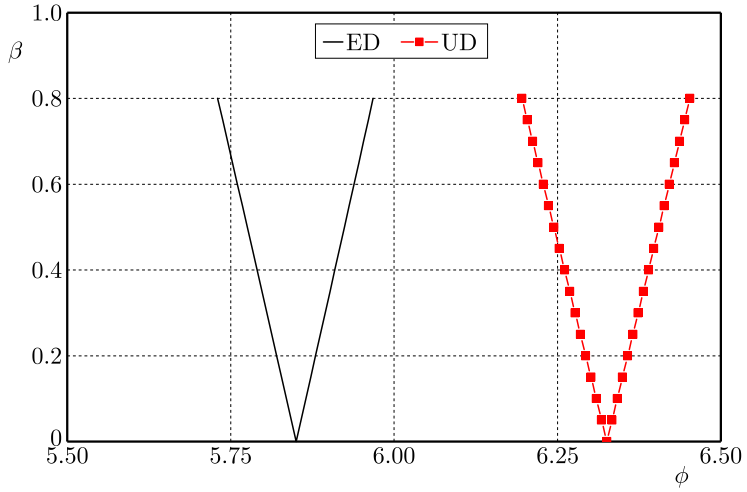

Fig. 5. Influence of porosity distribution on the dynamic stability of a porous S-FGM conical shell.

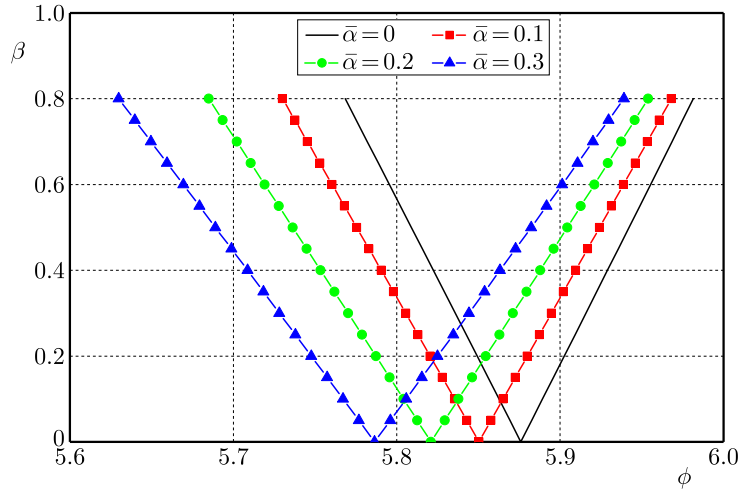

Fig. 6. Influence of porosity volume fraction on the dynamic stability of a porous S-FGM conical shell.

of SUS304, increasing W_c results in the rise of the effective stiffness. Also, the figure shows that the impact of the ceramic mass fraction W_c on the unstable region is insignificant and may be neglected.

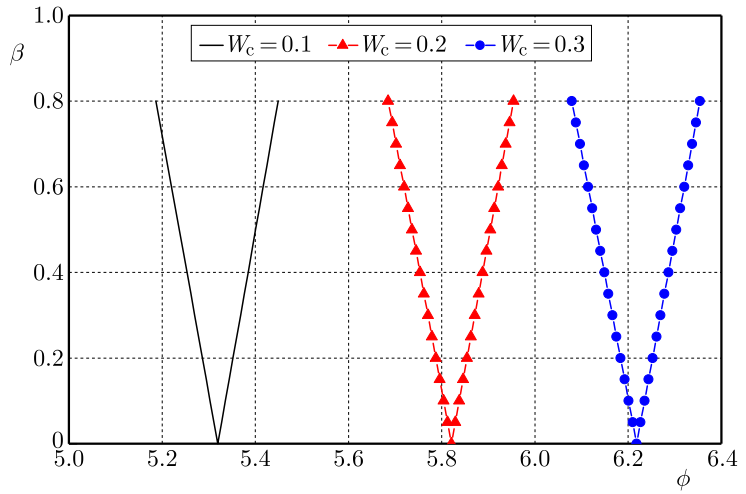

Fig. 7. Influence of ceramic mass fraction W_c on the dynamic stability for a porous S-FGM conical shell.

Figure 8 and Fig. 9 reveal the influences of the hydraulic and axial pressures, respectively. It can be observed that the influence of the hydraulic pressure on the dynamic stability may be neglected. Compared with the influence of the hydraulic pressure, that of the axial static

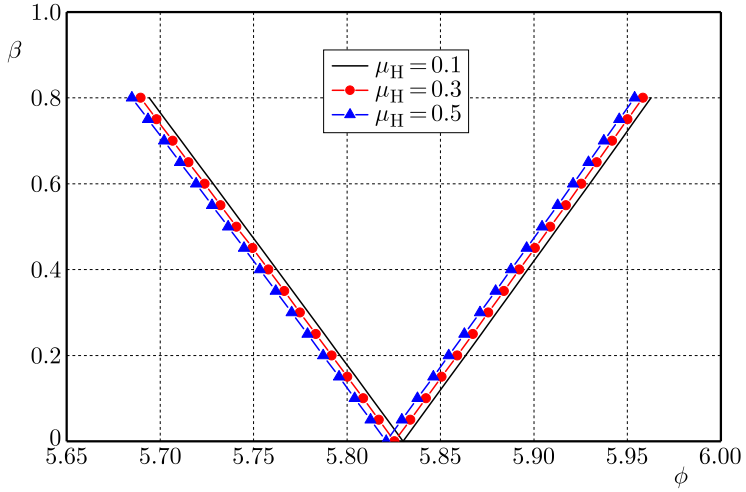

Fig. 8. Influence of hydraulic pressure on the dynamic stability for a porous S-FGM conical shell.

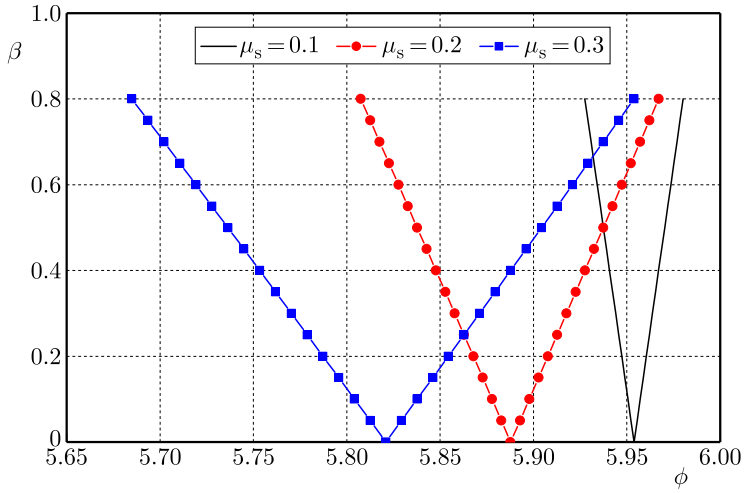

Fig. 9. Influence of the static axial pressure on the dynamic stability for a porous S-FGM conical shell.

loading is more significant. When the axial loading coefficient μ_s rises from 0.1 to 0.3, the critical excitation frequency ϕ^* declines from 5.954 to 5.821, and the subtended angle Θ increases from 1.88° to 9.48°. It is because the axial loading significantly weakens the effective stiffness, which leads to the decrease in the critical excitation frequency.

The influence of the fraction index N on the dynamic stability is illustrated in Fig. 10. From the figure, it can be observed that increasing the index N makes the critical excitation frequency ϕ^* decline. On the contrary, the subtended angle Θ declines with the increasing fraction index N. That is because the elastic modulus of Si_3N_4 is higher than that of SUS304, while its density is lower than that of Ni. Thus, the critical excitation frequency ϕ^* is decreased if the index N rises.

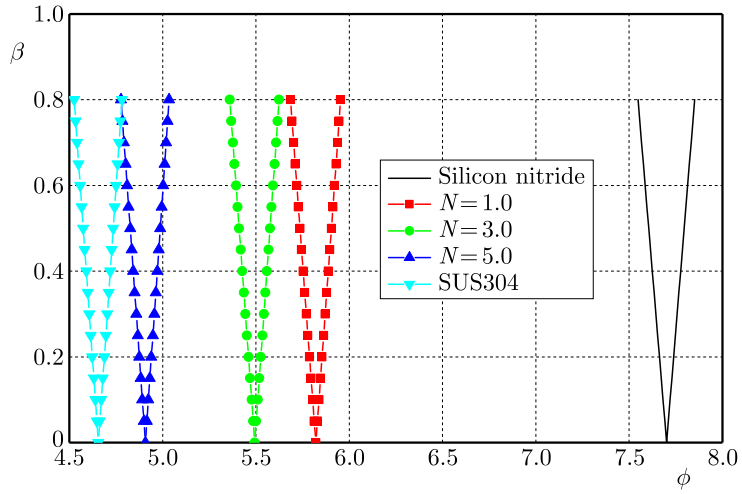

Fig. 10. Influence of the material fraction index N on the dynamic stability for a porous S-FGM conical shell.

Figure 11 reveals the influence of the elastic media, including the Winkler elastic medium ($k_w \neq 0$, $k_p = 0$), Pasternak elastic medium ($k_w = 0$, $k_p \neq 0$), and Winkler–Pasternak elastic medium ($k_w \neq 0$, $k_p \neq 0$). Since the effective stiffness can be enhanced by increasing the values of these parameters, it is seen that increasing these parameters makes the critical excitation frequency ϕ^* rise. However, the effect of the elastic medium parameters on the subtended angle Θ is very small and may be neglected.

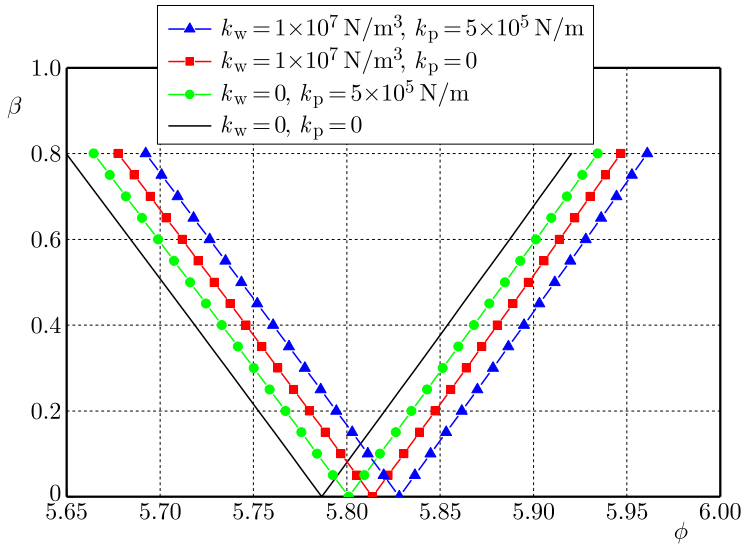

Fig. 11. Influence of elastic medium on the dynamic stability for a porous S-FGM conical shell.

The influences of the shell parameters, including half-vertex angle γ and the ratios R_1/h and L/R_1, on the dynamic stability are presented in Fig. 12, Fig. 13, and Fig. 14. In Fig. 12, it is illustrated that increasing the angle γ makes the critical excitation frequency ϕ^* decline. However,

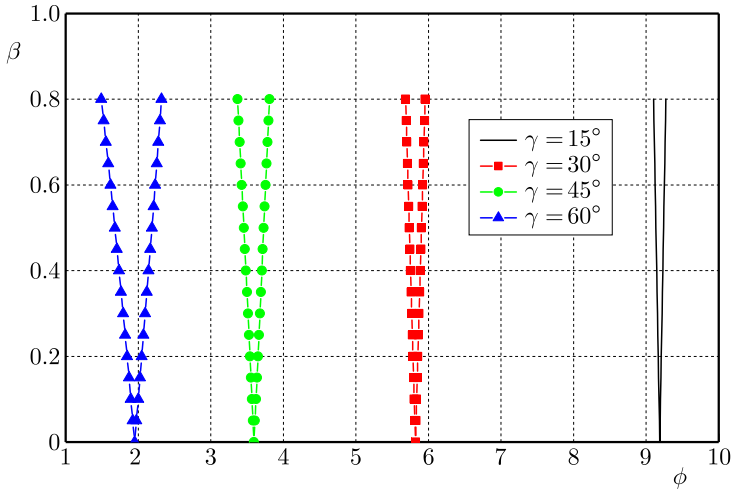

Fig. 12. Influence of the half-vertex angle γ on the dynamic stability for a porous S-FGM conical shell.

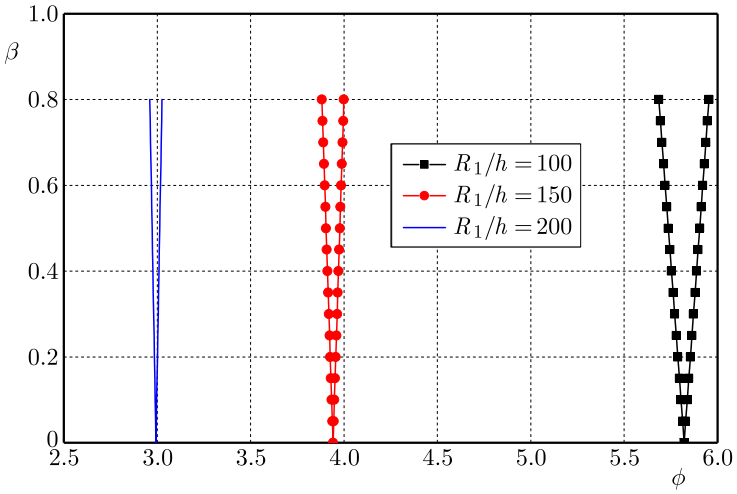

Fig. 13. Influence of the ratio R_1/h on the dynamic stability for a porous S-FGM conical shell.

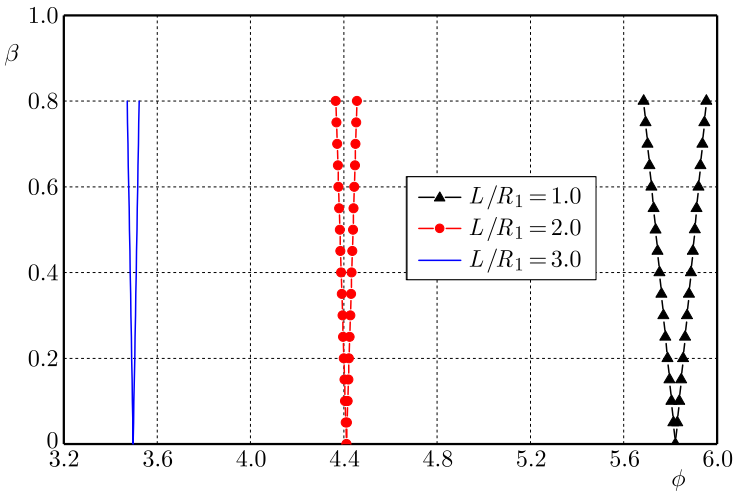

Fig. 14. Influence of the ratio L/R_1 on the dynamic stability for a porous S-FGM conical shell.

the subtended angle Θ increases as the half-vertex angle γ rises. The changes demonstrate that increasing γ can weaken the dynamic stability of the shell.

As shown in Fig. 13, the critical excitation frequency ϕ^* decreases with the rising ratio R_1/h. If the ratio R_1/h rises from 100 to 200, the frequency ϕ^* decreases from 5.820 to 3.941, whereas Θ increases from 9.53° to 39.43°. It is because the effective stiffness for a thick shell is larger than that for a thin shell. In addition, the impact of the ratio L/R_1 on the dynamic stability is revealed in Fig. 14. It is shown that the critical excitation frequency ϕ^* decreases from 5.821 to 3.497 as the L/R_1 changes from 1.0 to 3.0. However, the subtended angle Θ reduces from 2.93° to 1.83° when the ratio L/R_1 rises from 1.0 to 3.0. It is illustrated that a short conical shell is more stable than a slender shell.

4. Conclusion and future work

This study develops an improved and reliable material parameter calculation model for porous sigmoid functionally graded materials (S-FGMs), which breaks through the traditional assumption that the porosity volume fraction is negligible in the volume calculation of FGM structures. Within a general linear dynamic stability framework, the governing equations for porous S-FGM truncated conical shells surrounded by a Winkler–Pasternak elastic medium and subjected to the combined action of static hydraulic pressure and periodic axial pressure are rigorously derived based on thin shell theory. By combining the Galerkin integral method with the Bolotin method, the critical excitation frequency ϕ^* and subtended angle Θ of the shells are accurately solved. A systematic parametric study is then conducted to reveal the influence laws and intrinsic mechanisms of key parameters. It is noteworthy that while the subsequent quantitative results are obtained for a specific set of parameters, the analytical model and solution procedure established herein are universal and can be directly applied to a wider range of engineering problems involving similar porous functionally graded shell structures. The study reveals the shifts of dynamic stability boundaries in the parameter space. Within the examined parameter ranges, the key conclusions are drawn as follows:

(i) Internal pores significantly affect the location and width of the unstable regions. Increasing the porosity volume fraction $\overline{\alpha}$ shifts the critical excitation frequency ϕ^* towards lower values, while it broadens the unstable region by increasing the subtended angle Θ.

(ii) Increasing the ceramic mass fraction W_c shifts the dynamic stability boundary towards higher excitation frequencies, causing ϕ^* to rise significantly. However, the impact of W_c on the subtended angle Θ is negligible within the studied range.

(iii) The value of the critical excitation frequency ϕ^* can be decreased by increasing the half-vertex angle γ and the ratios R_1/h and L/R_1. In contrast to the ratios R_1/h and L/R_1, an increase in the half-vertex angle γ can enhance the value of the subtended angle Θ.

In general, based on the linear dynamic stability framework, this study uncovers the basic dynamic stability characteristics and the action mechanisms of key parameters of porous S-FGM truncated conical shells under combined loads. The established material parameter model, dynamic stability governing equations, and solution methodology provide a solid theoretical basis for the dynamic stability analysis of this novel gradient porous shell structure. Meanwhile, this research is restricted to linear analysis, simplified porosity models, single boundary and load conditions, as well as linear elastic constitutive assumptions, which clearly points out the direction for subsequent in-depth research. Future studies may focus on nonlinear dynamic stability analysis, improvement of the pore microscopic model, expansion of complex engineering conditions, optimization of the material constitutive model, and experimental verification, so as to further improve the dynamic stability analysis system of porous S-FGM truncated conical shells.

Appendix

In Eqs. (2.19) and (2.20), the differential operators $T_{ij}(\ )$ are defined as

$$
\begin{aligned}
T_{11}(F_1) &= A_2 e^{2x}\left(\frac{\partial^4 F_1}{\partial x^4} - 4\frac{\partial^3 F_1}{\partial x^3} + 4\frac{\partial^2 F_1}{\partial x^2} + 2\frac{\partial^2 F_1}{\partial \psi^2} + \frac{\partial^4 F_1}{\partial \psi^4}\right) \\
&\quad + s_1 e^{3x}\cot\gamma\left(\frac{\partial^2 F_1}{\partial x^2} + 3\frac{\partial F_1}{\partial x} + 2F_1\right) \\
&\quad + 2(A_1 - A_5)e^{2x}\left(\frac{\partial^4 F_1}{\partial x^2 \partial \psi^2} - 2\frac{\partial^3 F_1}{\partial x \partial \psi^2} + \frac{\partial^2 F_1}{\partial \psi^2}\right), \\
T_{12}(W) &= -A_3\left(\frac{\partial^4 W}{\partial x^4} - 4\frac{\partial^3 W}{\partial x^3} + 4\frac{\partial^2 W}{\partial x^2} + 2\frac{\partial^2 W}{\partial \psi^2} + \frac{\partial^4 W}{\partial \psi^4}\right) \\
&\quad - 2(A_4 + A_6)\left(\frac{\partial^4 W}{\partial x^2 \partial \psi^2} - 2\frac{\partial^3 W}{\partial x \partial \psi^2} + \frac{\partial^2 W}{\partial \psi^2}\right) \\
&\quad - s_1^4 e^{4x} k_{\mathrm{w}} W + s_1^2 e^{2x} k_{\mathrm{p}}\left(\frac{\partial^2 W}{\partial x^2} + \frac{\partial^2 W}{\partial \psi^2}\right), \\
T_{13}(W) &= -\frac{1}{2}s_1^3 e^{3x}\tan\gamma\left(-\frac{\partial W}{\partial x} + \frac{\partial^2 W}{\partial x^2}\right) - s_1^3 e^{3x}\tan\gamma\frac{\partial^2 W}{\partial \psi^2} - s_1^3 e^{3x}\tan\gamma\frac{\partial W}{\partial x}, \\
T_{14}(W) &= -\frac{1}{2}s_1 s_2^2 e^{x}\tan\gamma\left(-\frac{\partial W}{\partial x} + \frac{\partial^2 W}{\partial x^2}\right), \\
T_{21}(F_1) &= B_1 e^{2x}\left(\frac{\partial^4 F_1}{\partial x^4} - 4\frac{\partial^3 F_1}{\partial x^3} + 4\frac{\partial^2 F_1}{\partial x^2} + 2\frac{\partial^2 F_1}{\partial \psi^2} + \frac{\partial^4 F_1}{\partial \psi^4}\right) \\
&\quad + 2(B_2 + B_5)e^{4x}\left(\frac{\partial^4 F_1}{\partial x^2 \partial \psi^2} + 2\frac{\partial^3 F_1}{\partial x \partial \psi^2} + \frac{\partial^2 F_1}{\partial \psi^2}\right), \\
T_{22}(W) &= -B_4 e^{-4x}\left(\frac{\partial^4 W}{\partial x^4} - 4\frac{\partial^3 W}{\partial x^3} + 4\frac{\partial^2 W}{\partial x^2} + 2\frac{\partial^2 W}{\partial \psi^2} + \frac{\partial^4 W}{\partial \psi^4}\right) \\
&\quad + 2(B_6 - B_3)\left(\frac{\partial^4 W}{\partial x^2 \partial \psi^2} - 2\frac{\partial^3 W}{\partial x \partial \psi^2} + \frac{\partial^2 W}{\partial \psi^2}\right) + s_1 e^{x}\cot\gamma\left(\frac{\partial^2 W}{\partial x^2} - \frac{\partial W}{\partial x}\right),
\end{aligned}
\tag{A.1}
$$

where coefficients A_i and B_i are defined by

$$
\begin{aligned}
A_1 &= c_{11}B_1 + c_{12}B_2, & A_2 &= c_{11}B_2 + c_{21}B_1, \\
A_3 &= c_{11}B_3 + c_{21}B_4 + c_{12}, & A_4 &= c_{11}B_4 + c_{21}B_3 + c_{22}, \\
A_5 &= c_{61}B_5, & A_6 &= c_{61}B_6 + c_{62}, \\
B_1 &= c_{10}D, & B_2 &= -c_{20}D, \\
B_3 &= (c_{20}c_{21} - c_{11}c_{10})D, & B_4 &= (c_{20}c_{11} - c_{21}c_{10})D, \\
B_5 &= 1/c_{60}, & B_6 &= c_{61}/c_{60}, \\
D &= 1/(c_{10}c_{10} - c_{20}c_{20}).
\end{aligned}
\tag{A.2}
$$

In Appendix (A.2), coefficients c_{ik} are defined as follows:

$$c_{1k} = \int_{-0.5h}^{0.5h} z^k \frac{E(z)}{1-\nu^2(z)} dz, \qquad c_{2k} = \int_{-0.5h}^{0.5h} z^k \frac{\nu(z)E(z)}{1-\nu^2(z)} dz,$$
$$c_{6k} = \int_{-0.5h}^{0.5h} z^k \frac{E(z)}{2(1+\nu(z))} dz. \tag{A.3}$$

Acknowledgments

The present research is funded by the financial support of the Natural Science Foundation of Guangxi (grant no. 2025GXNSFAA069217) and (grant no. 2021GXNSFAA220087) and the National Natural Science Foundation of China (grant no. 12162010). The authors are grateful for their support.

References

1. Ali, A.Y., & Hasan, H.M. (2019). Nonlinear dynamic stability of an imperfect shear deformable orthotropic functionally graded material toroidal shell segments under the longitudinal constant velocity. *Proceedings of the Institution of Mechanical Engineers, Part C: Journal of Mechanical Engineering Science*, *233*(19–20), 6827–6850. https://doi.org/10.1177/0954406219867991
2. Allahkarami, F., Saryazdi, M.G., & Tohidi, H. (2020). Dynamic buckling analysis of bi-directional functionally graded porous truncated conical shell with different boundary conditions. *Composite Structures*, *252*, Article 112680. https://doi.org/10.1016/j.compstruct.2020.112680
3. Bich, D.H., & Ninh, D.G. (2016). Post-buckling of sigmoid-functionally graded material toroidal shell segment surrounded by an elastic foundation under thermo-mechanical loads. *Composite Structures*, *138*, 253–263. https://doi.org/10.1016/j.compstruct.2015.11.044
4. Chi, S.-H., & Chung, Y.-L. (2006). Mechanical behavior of functionally graded material plates under transverse load—Part I: Analysis. *International Journal of Solids and Structures*, *43*(13), 3657–3674. https://doi.org/10.1016/j.ijsolstr.2005.04.011
5. Duc, N.D., & Cong, P.H. (2015). Nonlinear dynamic response of imperfect symmetric thin sigmoid-functionally graded material plate with metal-ceramic-metal layers on elastic foundation. *Journal of Vibration and Control*, *21*(4), 637–646. https://doi.org/10.1177/1077546313489717
6. Duc, N.D., Kim, S.E., & Chan, D.Q. (2018). Thermal buckling analysis of FGM sandwich truncated conical shells reinforced by FGM stiffeners resting on elastic foundations using FSDT. *Journal of Thermal Stresses*, *41*(3), 331–365. https://doi.org/10.1080/01495739.2017.1398623
7. Fan, L.J., Sahmani, S., & Safaei, B. (2021). Couple stress-based dynamic stability analysis of functionally graded composite truncated conical microshells with magnetostrictive facesheets embedded within nonlinear viscoelastic foundations. *Engineering with Computers*, *37*(2), 1635–1655. https://doi.org/10.1007/s00366-020-01182-w
8. Foroutan, K., & Torabi, F. (2026). Nonlinear chaotic and periodic responses of obliquely stiffened sigmoid FG cylindrical shells under principal torsional parametric, subharmonic, and 1:2 internal resonances. *Thin-Walled Structures*, *221*, Article 114463. https://doi.org/10.1016/j.tws.2025.114463
9. Fu, T., Wu, X., Xiao, Z., & Chen, Z. (2021). Dynamic instability analysis of porous FGM conical shells subjected to parametric excitation in thermal environment within FSDT. *Thin-Walled Structures*, *158*, Article 107202. https://doi.org/10.1016/j.tws.2020.107202
10. Hoa, L.K., Phi, B.G., Chan, D.Q., & Hieu, D.V. (2022). Buckling analysis of FG porous truncated conical shells resting on elastic foundations in the framework of the shear deformation theory. *Advances in Applied Mathematics and Mechanics*, *14*(1), 218–247. https://doi.org/10.4208/aamm.OA-2020-0202

11. Mallek, H., Mellouli, H., Ben Said, L., Wali, M., Dammak, F., & Alhadri, M. (2025). Porosity effects on nonlinear static performances of functionally graded shells considering thickness stretching. *Facta Universitatis, Series: Mechanical Engineering*, *23*(4), 827–860. https://doi.org/10.22190/FUME240920015M

12. Naj, R., Sabzikar Boroujerdy, M., & Eslami, M.R. (2008). Thermal and mechanical instability of functionally graded truncated conical shells. *Thin-Walled Structures*, *46*(1), 65–78. https://doi.org/10.1016/j.tws.2007.07.011

13. Nemati, A.R., & Mahmoodabadi, M.J. (2020). Effect of micromechanical models on stability of functionally graded conical panels resting on Winkler–Pasternak foundation in various thermal environments. *Archive of Applied Mechanics*, *90*(5), 883–915. https://doi.org/10.1007/s00419-019-01646-6

14. Ng, T.Y., Lam, K.Y., Liew, K.M., & Reddy, J.N. (2001). Dynamic stability analysis of functionally graded cylindrical shells under periodic axial loading. *International Journal of Solids and Structures*, *38*(8), 1295–1309. https://doi.org/10.1016/S0020-7683(00)00090-1

15. Pal, S., Rout, M., Deb Singha, T., & Karmakar, A. (2025). Thermoelastic free vibration of rotating pretwisted porous p-FGM, e-FGM, and s-FGM conical shells in nonlinear temperature distribution. *Journal of Vibration and Control*, *31*(7–8), 1258–1277. https://doi.org/10.1177/10775463241240625

16. Sofiyev, A.H. (2009). The vibration and stability behavior of freely supported FGM conical shells subjected to external pressure. *Composite Structures*, *89*(3), 356–366. https://doi.org/10.1016/j.compstruct.2008.08.010

17. Sofiyev, A.H. (2010). The buckling of FGM truncated conical shells subjected to combined axial tension and hydrostatic pressure. *Composite Structures*, *92*(2), 488–498. https://doi.org/10.1016/j.compstruct.2009.08.033

18. Sofiyev, A.H. (2016). Parametric vibration of FGM conical shells under periodic lateral pressure within the shear deformation theory. *Composites Part B: Engineering*, *89*, 282–294. https://doi.org/10.1016/j.compositesb.2015.11.017

19. Sofiyev, A.H., Alizada, A.N., Akin, Ö., Valiyev, A., Avcar, M., & Adiguzel, S. (2012). On the stability of FGM shells subjected to combined loads with different edge conditions and resting on elastic foundations. *Acta Mechanica*, *223*(1), 189–204. https://doi.org/10.1007/s00707-011-0548-1

20. Sofiyev, A.H., & Schnack, E. (2012). The vibration analysis of FGM truncated conical shells resting on two-parameter elastic foundations. *Mechanics of Advanced Materials and Structures*, *19*(4), 241–249. https://doi.org/10.1080/15376494.2011.642934

21. Wu, H., Yang, J., & Kitipornchai, S. (2020). Mechanical analysis of functionally graded porous structures: A review. *International Journal of Structural Stability and Dynamics*, *20*(13), Article 2041015. https://doi.org/10.1142/S0219455420410151

22. Yuan, Y., Zhao, X., Zhao, Y., Sahmani, S., & Safaei, B. (2021). Dynamic stability of nonlocal strain gradient FGM truncated conical microshells integrated with magnetostrictive facesheets resting on a nonlinear viscoelastic foundation. *Thin-Walled Structures*, *159*, Article 107249. https://doi.org/10.1016/j.tws.2020.107249

23. Zhang, J., & Li, S. (2010). Dynamic buckling of FGM truncated conical shells subjected to non-uniform normal impact load. *Composite Structures*, *92*(12), 2979–2983. https://doi.org/10.1016/j.compstruct.2010.05.009

24. Zhu, J., Lai, Z., Yin, Z., Jeon, J., & Lee, S. (2001). Fabrication of ZrO_2–NiCr functionally graded material by powder metallurgy. *Materials Chemistry and Physics*, *68*(1–3), 130–135. https://doi.org/10.1016/S0254-0584(00)00355-2

Manuscript received November 5, 2025; accepted for publication June 13, 2026; published online June 22, 2026.